Two-phase nanofluid over rotating disk with exponential variable thickness

Liu, Chunyan; Ding, Yiming; Zheng, Liancun; Lin, Ping; Li, Ruilin

Published in:
International Journal of Numerical Methods for Heat and Fluid Flow

DOI:
10.1108/HFF-07-2018-0347

Publication date:
2019

Document Version
Peer reviewed version

Two-phase nanofluid over rotating disk with exponential variable thickness

Chunyan Liu[a], Yiming Ding[c], Liancun Zheng[a,*], Ping Lin[b], Ruilin Li[a]

[a] *School of Mathematics and Physics, University of Science and Technology Beijing, Beijing 100083, China*
[b] *Division of Mathematics, University of Dundee, Dundee DD1 4HN, Scotland, United Kingdom*
[c] *School of Energy and Environmental Engineering, University of Science and Technology Beijing, Beijing 100083, China*

Abstract

Purpose - The purpose of this paper is to investigate the effect of nanofluid over rotating disk with the exponential variable thickness $Z = ce^{-\frac{bR}{R_0}}, (c > 0, b > 0)$ and to analyze Brownian motion and thermophoresis of Buongiorno model on the disk embedded in nanofluid-saturated porous media.
Design/methodology/approach - Employing the generalized Von Karman transformation, the boundary layer governing equations are transformed into semi-similar forms solved by bvp4c in Matlab.
Findings - The effects of the thickness parameter a, the shape parameter b, the Brownian motion parameter Nb and thermophoresis parameter Nt on flow, heat and mass transfer are analyzed. With the increase of thickness parameter a, the radial velocity first decreases and then increases, showing the opposite trend on the two sides of the peak value. Moreover, temperature and concentration rise as the Brownian motion parameter becomes larger.
Originality/value - It is the first work that has been done on rotating disk with exponential variable thickness in nanofluid. The impact of the two slip effects, namely, Brownian motion and thermophoresis, on the nanofluid boundary layer flow, heat and mass transfer due to rotating disk with exponential variable thickness $Z = ce^{-\frac{bR}{R_0}}, (c > 0, b > 0)$ has been addressed in this study.
Keyword - Variable thickness rotating disk, Nanofluid, Generalized Von Karman transformation, Porous media
Paper type - Research paper

1. Introduction

Nanofluid has received wide attention due to its high thermal conductivity and heat transfer capability. The concept of nanofluid was first proposed by Choi and Eastman in 1995

*Corresponding author.Tel.:+86(10)6233 2002
Email address: liancunzheng@ustb.edu.cn, liancunzheng@163.com (Liancun Zheng)

[1]. Eastman et al. (2001) [2] focused on higher thermal conductivities of ethylene glycol-based nanofluids containing copper nanoparticles instead of oxide nanoparticles. Buongiorno (2006) [3] investigated seven possible slip mechanisms with relative velocity between the nanoparticles and the base fluid and concluded that Brownian motion and thermophoresis are the most important slip mechanisms in nanofluid. The above research stimulated the scholars to Brownian motion and thermophoresis on two-phase nanofluid. Kuznetsov and Nield (2010) [4] studied the natural convective flow of a nanofluid past a vertical plate. Sheikholeslami et al. (2013) [5] depicted two-phase simulation of nanofluid flow and heat transfer. Reddy and Chamkha (2017) [6] studied natural convection flow of nanofluid along a vertical cone with chemical reaction. More literatures on nanofluid flow and heat transfer have been presented in Refs.(Nield and Kuznetsov, 2009; Mohsen et al., 2014; Chamkha et al., 2015; Zhang et al., 2016, 2017; Wakif et al. 2018) [7–11].

The problem of the flow and heat transfer in porous media is important in many industrial fields, such as food processing, geothermal extraction, and diffusion of underground pollutants. Darcy put forward the transport phenomena in porous media for the first time in 1856 (Khayargoli et al, 2004) [12]. Later, Yih (1998) [13] studied the effect of uniform suction/blowing on forced MHD Hiemenz flow in a porous medium against a variable wall temperature plate. Chamkha and Al-Humoud (2007) [14] presented mixed convection of a power-law fluid over a vertical plate embedded in a fluid-saturated porous medium. Hassanien and Al-Arabi (2009) [15] considered the unsteady stagnation point flow near a heated vertical plate in a porous medium. Chamkha et al. (2014) [16] investigated heat and mass transfer with Soret and Dufour effects through a porous medium under the inclined magnetic field. Barnoon and Toghraie (2018) [17] showed heat transfer of kerosene/MWCNT nanofluid in a double-layer microchannel through a porous medium.

Flow induced by the rotation of disk has been used in the field of engineering and technology such as turbine, aircraft propeller, and centrifugal pump. The governing equations of steady flow on rotating disk were originally reduced to similarity forms by Karman (1921) [18]. Based on this work, Millsaps and Pohlhausen (1951) [19] considered laminar flow and heat transfer from a rotating-plate by Keller box method. Ackroyd (1978) [20] investigated series solution of rotating disk flow with either surface suction or injection. The influence of porous media on the steady flow due to a rotating disk was examined in (Turkyilmazoglu, 2010; Devi and Devi, 2012; Rashidi et al., 2013; Khan et al., 2016) [21–24]. The fluid flow model on the rotating disk is more mature.

Recently, Xun et al. (2016) [25] studied power-law fluids over a variable thickness rotating disk with index decreasing by Runge-Kutta method coupled with multi-shooting technique. Hayat et al. (2017) [26] reported nanofluid flow with homogeneous-heterogeneous reactions due to rotating disk with variable thickness through the homotopy analysis method (HAM). Several recent studies on the modeling of variable thickness rotating disk with index decreasing have been discussed by Hayat et al. (2017; 2018; 2018) [27–29]. On the other hand, Liu et al. (2016) [30] investigated approximate analytical solutions of Bingham fluid over a variable thickness rotating disk with exponential decreasing by HAM. The above-mentioned works are based on the similarity transformation method, and then numerical or analytical solutions are obtained to solve a set of ordinary differential equations. Also there exist some

novel methods which can be used to solve the boundary layer problems directly (Mirzaei and Dehghan, 2012; Dehghan and Abbaszadeh, 2016; 2017; Kamranian et al., 2017; Dehghan and Abbaszadeh, 2018)[31–35]. To the best of our knowledge, very few studies have been conducted for investigating rotating disk with exponential variable thickness flow problems.

Motivated by the discussions mentioned above, it is meaningful to investigate flow, heat and mass transfer of two-phase nanofluid model over rotating disk with exponential variable thickness in porous media. Boundary layer governing partial equations are solved by the generalized Von Karman transformation and bvp4c in Matlab. Impacts of pertinent parameters on velocity, temperature and concentration fields are discussed by displaying figures and tables. Moreover, physical quantities at the disk (local Nusselt number and local Sherwood number) are discussed graphically. The structure of the paper is as follows:
In Section 2, the governing equations of model and generalized Von-Karman transformations are highlighted.
In Section 3, the numerical results and discussions are given.
Finally, the conclusions are eventually summarized in Section 4.

Nomenclature

a	=thickness parameter, $(a > 0)$, $[-]$
b	=shape parameter, $(b > 0)$, $[-]$
c	=variable thickness parameter, $[m]$
C	=concentration, $[kg\ m^{-3}]$
C_{fr}	=local skin-friction coefficient, $[-]$
C_∞	=ambient concentration, $[kg\ m^{-3}]$
D_B	=Brownian diffusion coefficient, $[m^2\ s^{-1}]$
D_T	=thermophoretic diffusion coefficient, $[m^2\ s^{-1}]$
k	=thermal conductivity, $[Wm^{-1}\ K]$
K	=permeability of porous medium, $[m^2]$
M	=permeability parameter, $[-]$
Nb	=Brownian motion parameter, $[-]$
Nt	=thermophoresis parameter, $[-]$
Nu_r	=local Nusselt number, $[-]$
P	=pressure, $[Pa]$
Pr	=Prandtl number, $[-]$
q_m	=mass flux, $[kg\ m^{-2}s^{-1}]$
q_W	=heat flux, $[W\ m^{-2}]$
R_0	=feature radius, $[m]$
Re	=Reynolds number, $[-]$
Sc	=Schmidt number, $[-]$
Sh_r	=local Sherwood number, $[-]$
T	=temperature, $[K]$
T_W	=temperature of disk, $[K]$
T_∞	=ambient temperature, $[K]$
(U,V,W)	=velocity in R,Φ,Z-axis direction, $[m\ s^{-1}]$
(R,Φ,Z)	=R,Φ,Z-axis, $[m]$
Greek symbols	
$(\rho c_p)_f$, $(\rho c_p)_s$	=heat capacity of fluid, nanoparticle, $[kg\ m^{-3}K]$
τ_{rz}, $\tau_{\phi z}$	=radial stress, tangential stress, $[N]$
τ	=nanoparticle heat capacity ratio, $[-]$
η	=similarity variable, $[-]$
ξ	=similarity variable after coordinate transformation, $[-]$
μ	=dynamic viscosity, $[Ns\ m^{-2}]$
ρ	=density, $[kg\ m^{-3}]$
ω	=constant angular velocity, $[s^{-1}]$
Subscripts	
W	=condition at the disk, $[-]$
∞	=ambient condition, $[-]$
f	=fluid, $[-]$
s	=nanoparticle, $[-]$
Superscripts	
$'$	=differentiation with respect to η or ξ, $[-]$

2. Mathematical model

Consider the steady incompressible three-dimensional flow of two-phase nanofluid on a radially variable thickness rotating disk with exponential decreasing form $Z = ce^{-\frac{bR}{R_0}}, (c > 0, b > 0)$ shown in Fig. 1, where c is the variable thickness parameter of disk, b is the shape parameter of disk. The disk embedded in nanofluid-saturated porous media is rotating about the Z-axis with constant angular velocity ω in the cylindrical coordinate system (R, Φ, Z). The continuity equation, momentum equation, energy equation and mass transfer equation in the boundary layer can be written as follows

$$\frac{\partial U}{\partial R} + \frac{U}{R} + \frac{\partial W}{\partial Z} = 0 \tag{1}$$

$$\rho\left(U\frac{\partial U}{\partial R} + W\frac{\partial U}{\partial Z} - \frac{V^2}{R}\right) = -\frac{\partial P}{\partial R} + \mu\left(\frac{\partial^2 U}{\partial R^2} + \frac{1}{R}\frac{\partial U}{\partial R} - \frac{U}{R^2} + \frac{\partial^2 U}{\partial Z^2}\right) - \frac{\mu}{K}U \tag{2}$$

$$\rho\left(U\frac{\partial V}{\partial R} + W\frac{\partial V}{\partial Z} + \frac{UV}{R}\right) = \mu\left(\frac{\partial^2 V}{\partial R^2} + \frac{1}{R}\frac{\partial V}{\partial R} - \frac{V}{R^2} + \frac{\partial^2 V}{\partial Z^2}\right) - \frac{\mu}{K}U \tag{3}$$

$$\begin{aligned}(\rho c_p)_f\left(U\frac{\partial T}{\partial R} + W\frac{\partial T}{\partial Z}\right) &= k\left(\frac{\partial^2 T}{\partial R^2} + \frac{1}{R}\frac{\partial T}{\partial R} + \frac{\partial^2 T}{\partial Z^2}\right)\\ +(\rho c_p)_s\left(D_B\left(\frac{\partial T}{\partial R}\frac{\partial C}{\partial R} + \frac{\partial T}{\partial Z}\frac{\partial C}{\partial Z}\right) + \frac{D_T}{T_\infty}\left(\left(\frac{\partial T}{\partial R}\right)^2 + \left(\frac{\partial T}{\partial Z}\right)^2\right)\right)\end{aligned} \tag{4}$$

$$U\frac{\partial C}{\partial R} + W\frac{\partial C}{\partial Z} = D_B\left(\frac{\partial^2 C}{\partial R^2} + \frac{1}{R}\frac{\partial C}{\partial R} + \frac{\partial^2 C}{\partial Z^2}\right) + \frac{D_T}{T_\infty}\left(\frac{\partial^2 T}{\partial R^2} + \frac{1}{R}\frac{\partial T}{\partial R} + \frac{\partial^2 T}{\partial Z^2}\right) \tag{5}$$

The relevant boundary conditions are

$$\begin{aligned}&Z = ce^{-\frac{bR}{R_0}} : U = 0, V = \omega R, W = 0, T = T_W, C = C_W\\ &Z \to \infty : U = 0, V = 0, T = T_\infty, C = C_\infty\end{aligned} \tag{6}$$

where U, V and W are velocity components in the directions of R, Φ, Z, respectively. T is the temperature, C is the concentration, ρ is the density and μ is the dynamic viscosity. k is the thermal conductivity, c_p is the specific heat of nanofluid, K is the permeability of the porous media. D_B is the Brownian diffusion coefficient, D_T is the thermophoretic diffusion coefficient, P is the pressure and R_0 is the feature radius. T_W is the temperature of disk and T_∞ is the temperature of ambient fluid. C_W is the concentration of disk and C_∞ is the concentration of ambient fluid.

The following dimensionless variables are introduced

$$\begin{gathered} r=\frac{R}{R_0}, z=\frac{Z}{R_0}, u=\frac{U}{\omega R_0}, v=\frac{V}{\omega R_0}, w=\frac{W}{\omega R_0}, t=\frac{T-T_\infty}{T_W-T_\infty}, \\ c'=\frac{C-C_\infty}{C_W-C_\infty}, \mathrm{Re}=\frac{\rho\omega {R_0}^2}{\mu}, M=\frac{{R_0}^2}{K}, \mathrm{Pr}=\frac{\mu c_p}{k}, \tau=\frac{(\rho c_p)_s}{(\rho c_p)_f}, \\ Nb=\frac{\tau\rho D_B\left(C_W-C_\infty\right)}{\mu}, Nt=\frac{\tau\rho D_T\left(T_W-T_\infty\right)}{\mu T_\infty}, Sc=\frac{\mu}{\rho D_B}, p=\frac{P}{\mu\omega} \end{gathered} \tag{7}$$

where Pr is the Prandtl number, Re is the Reynolds number, Sc is the Schmidt number and M is the permeability parameter. Nb is the Brownian motion parameter and Nt is the thermophoresis parameter and τ is the ratio between the effective heat capacity of the nanoparticle and heat capacity of the fluid.

Eqs. (1)-(6) are reduced to the following system of equations by using Eq. (7):

$$\frac{\partial u}{\partial r}+\frac{u}{r}+\frac{\partial w}{\partial z}=0 \tag{8}$$

$$Re\left(u\frac{\partial u}{\partial r}+w\frac{\partial u}{\partial z}-\frac{v^2}{r}\right)=-\frac{\partial p}{\partial r}+\frac{\partial^2 u}{\partial r^2}+\frac{1}{r}\frac{\partial u}{\partial r}-\frac{u}{r^2}+\frac{\partial^2 u}{\partial z^2}-Mu \tag{9}$$

$$Re\left(u\frac{\partial v}{\partial r}+w\frac{\partial v}{\partial z}+\frac{uv}{r}\right)=\frac{\partial^2 v}{\partial r^2}+\frac{1}{r}\frac{\partial v}{\partial r}-\frac{v}{r^2}+\frac{\partial^2 v}{\partial z^2}-Mv \tag{10}$$

$$\begin{gathered} Re\left(u\frac{\partial t}{\partial r}+w\frac{\partial t}{\partial z}\right)=\frac{1}{\mathrm{Pr}}\left(\frac{\partial^2 t}{\partial r^2}+\frac{1}{r}\frac{\partial t}{\partial r}+\frac{\partial^2 t}{\partial z^2}\right) \\ +Nb\left(\frac{\partial t}{\partial r}\frac{\partial c'}{\partial r}+\frac{\partial t}{\partial z}\frac{\partial c'}{\partial z}\right)+Nt\left(\left(\frac{\partial t}{\partial r}\right)^2+\left(\frac{\partial t}{\partial z}\right)^2\right) \end{gathered} \tag{11}$$

$$ReSc\left(u\frac{\partial c'}{\partial r}+w\frac{\partial c'}{\partial z}\right)=\left(\frac{\partial^2 c'}{\partial r^2}+\frac{1}{r}\frac{\partial c'}{\partial r}+\frac{\partial^2 c'}{\partial z^2}\right)+\frac{Nt}{Nb}\left(\frac{\partial^2 t}{\partial r^2}+\frac{1}{r}\frac{\partial t}{\partial r}+\frac{\partial^2 t}{\partial z^2}\right) \tag{12}$$

subject to the boundary conditions

$$\begin{gathered} z=ae^{-br}: u=0, v=r, w=0, t=1, c'=1 \\ z\to\infty: u=0, v=0, t=0, c'=0 \end{gathered} \tag{13}$$

where $a=c/R_0$ is the variable thickness parameter.

Consider the generalized Von-Karman transformations

$$\eta=e^{br}z, u=rF\left(\eta\right), v=rG\left(\eta\right), w=e^{-br}H\left(\eta\right), t=\varphi\left(\eta\right), c'=\theta\left(\eta\right) \tag{14}$$

where η is similarity variable. Substituting Eq. (14) in Eqs. (8)-(13), we obtain the following system of semi-similarity equations:

$$2F+rF'b\eta+H'=0 \tag{15}$$

$$\mathrm{Re}\left(F^2+rFF'b\eta+HF'-G^2\right)=(b+\frac{3}{r})F'b\eta+F''\left(b^2\eta^2+e^{2br}\right)-MF \tag{16}$$

$$\mathrm{Re}\left(rFG'b\eta+G'H+2FG\right)=(b+\frac{3}{r})G'b\eta+G''\left(b^2\eta^2+e^{2br}\right)-MG \tag{17}$$

$$\mathrm{Re}\left(rFb\eta+H\right)\varphi'=\frac{1}{\mathrm{Pr}}\left(\left(b^2\eta^2+e^{2br}\right)\varphi''+(b+\frac{1}{r})\varphi'b\eta\right)+\left(Nb\varphi'\theta'+Nt(\varphi')^2\right)\left(b^2\eta^2+e^{2br}\right) \tag{18}$$

$$ReSc\left(rFb\eta+H\right)\theta'=\left(\theta''\left(b^2\eta^2+e^{2br}\right)+(b+\frac{1}{r})\theta'b\eta\right)+\frac{Nt}{Nb}\left(\varphi''\left(b^2\eta^2+e^{2br}\right)+(b+\frac{1}{r})\varphi'b\eta\right) \tag{19}$$

The transformed boundary conditions become

$$\begin{array}{l}\eta=a:F=0,G=1,H=0,\varphi=1,\theta=1,\\ \eta\to\infty:F=0,G=0,\varphi=0,\theta=0\end{array} \tag{20}$$

where a is the thickness parameter, and $\eta=a$ indicates the rotating disk surface. The prime denotes derivative with respect to η.

In order to facilitate the computation, we define

$$\begin{array}{c}F(\eta)=f(\eta-a)=f(\xi),G(\eta)=g(\eta-a)=g(\xi),H(\eta)=h(\eta-a)=h(\xi),\\ \varphi(\eta)=s(\eta-a)=s(\xi),\theta(\eta)=q(\eta-a)=q(\xi)\end{array} \tag{21}$$

Eqs.(15)-(20) become

$$2f+rf'b\left(\xi+a\right)+h'=0 \tag{22}$$

$$Re\left(f^2+rff'b\left(\xi+a\right)+f'h-g^2\right)=(b+\frac{3}{r})f'b\left(\xi+a\right)+f''\left(b^2(\xi+a)^2+e^{2br}\right)-Mf \tag{23}$$

$$Re\left(rfg'b\left(\xi+a\right)+g'h+2fg\right)=(b+\frac{3}{r})g'b\left(\xi+a\right)+g''\left(b^2(\xi+a)^2+e^{2br}\right)-Mg \tag{24}$$

$$\begin{array}{r}Re\left(rfb\left(\xi+a\right)+h\right)s'=\frac{1}{\mathrm{Pr}}\left(\left(b^2(\xi+a)^2+e^{2br}\right)s''+(b+\frac{1}{r})b\left(\xi+a\right)s'\right)\\ +\left(Nbs'q'+Nt(s')^2\right)\left(b^2(\xi+a)^2+e^{2br}\right)\end{array} \tag{25}$$

$$ReSc\left(rfb\left(\xi+a\right)+h\right)q'=\left(\left(b^2(\xi+a)^2+e^{2br}\right)q''+(b+\frac{1}{r})b\left(\xi+a\right)q'\right)\\+\frac{Nt}{Nb}\left(\left(b^2(\xi+a)^2+e^{2br}\right)s''+(b+\frac{1}{r})b\left(\xi+a\right)s'\right) \tag{26}$$

with these boundary conditions

$$f\left(0\right)=0,g\left(0\right)=1,h\left(0\right)=0,s\left(0\right)=1,q\left(0\right)=1\\f\left(\infty\right)=0,g\left(\infty\right)=0,s\left(\infty\right)=0,q\left(\infty\right)=0 \tag{27}$$

where the prime denotes the differentiation with respect to the similarity variable ξ.

Quantities of practical interest in this model are the local skin-friction coefficient C_{fr}, the local Nusselt number Nu_r and the local Sherwood number Sh_r. These are defined by

$$C_{fr}=\frac{\sqrt{\tau_{rz}^2+\tau_{\phi z}^2}}{\rho(R\omega)^2},Nu_r=\frac{Rq_W}{k\left(T_W-T_\infty\right)},Sh_r=\frac{Rq_m}{D_B\left(C_W-C_\infty\right)} \tag{28}$$

Further the radial stress τ_{rz}, tangential stress $\tau_{\phi z}$, heat flux q_W and mass flux q_m are obtained as follows:

$$\tau_{rz}=\mu\left(\frac{\partial U}{\partial Z}+\frac{\partial W}{\partial R}\right)\Big|_{Z=ce^{-\frac{bR}{R_0}}},\tau_{\phi z}=\mu\left(\frac{\partial V}{\partial Z}+\frac{1}{R}\frac{\partial W}{\partial\Phi}\right)\Big|_{Z=ce^{-\frac{bR}{R_0}}},\\q_W=-k\frac{\partial T}{\partial Z}\Big|_{Z=ce^{-\frac{bR}{R_0}}},q_m=-D_B\frac{\partial C}{\partial Z}\Big|_{Z=ce^{-\frac{bR}{R_0}}} \tag{29}$$

Substituting Eq. (29) in Eq. (28), we obtain

$$C_{fr}=\frac{e^{br}\sqrt{\left(rf'\left(0\right)+e^{-2br}b\left(ah'\left(0\right)-h\left(0\right)\right)\right)^2+\left(rg'\left(0\right)\right)^2}}{Rer^2},\\Nu_r=-rs'\left(0\right)e^{br},Sh_r=-rq'\left(0\right)e^{br}. \tag{30}$$

3. Results and Discussions

The flow, heat and mass transfer of two-phase model of nanofluid over a rotating disk with variable thickness radially through porous media are studied. The set of nonlinear ordinary differential Eqs. (22)-(27) are solved by bvp4c in Matlab. A comparison among previous results given by Turkyilmazoglu (2010) [21], Rashidi et al. (2013) [23] and our results of Newtonian fluid is illustrated in Table 1. An excellent agreement in all results is found. Table 2 presents the used CPU times for the presented method with different Re. For the sake of simplicity, Prandtl number is 1 and Schmidt number is 1. The effects of other physical parameters, namely permeability parameter M, thickness parameter a, shape

parameter b, Brownian motion parameter Nb and thermophoresis parameter Nt on flow, heat, and mass transfer are discussed.

The variation of the radial velocity profiles for different values of the thickness parameter a and permeability parameter M is shown in Fig. 2. With the increase of the thickness parameter a, the maximum value of the radial velocity profile remarkably reduces, but the thickness of momentum boundary layer increases slightly in Fig. 2 (a). The influence of the permeability parameter M on the component of radial velocity is depicted in Fig. 2 (b). With the increase of the permeability parameter M, both radial velocity and thickness of momentum boundary layer decrease.

The dependence of the radial and tangential velocity profiles on different values of the shape parameter b is shown in Fig. 3. Fig. 3 (a) indicates the radial velocity first decreases and then increases, showing the opposite distribution around the peak value for the increase of shape parameter b. Moreover, as the shape parameter b becomes larger, the thickness of the radial velocity boundary layer is thicker and the peak value of the radial velocity is far from the disk. An increase in thickness parameter b corresponds to lager tangential velocity and thicker thickness of the tangential velocity boundary layer as shown in Fig. 3 (b). That is to say, physically, the increase of the steepness of the disk promotes the radial and tangential velocity.

The variation of the axial velocity profiles for different values of the thickness parameter a and permeability parameter M is plotted in Fig. 4. Fig. 4 (a) shows the axial velocity increases with the increase of the thickness parameter a until it is close to the maximum and is maintained, where the axial velocity decreases with augment of the thickness parameter a. It is noteworthy that the thickness of axial velocity boundary layer decreases with the thicker disk. Fig. 4 (b) discloses the axial velocity and its boundary layer thickness both decrease with the increase of the permeability parameter M in the entire boundary layer. From the physical point of view, the flow resistance of porous media restrains the axial velocity.

The dependence of the temperature profiles for different values on the Brownian motion parameter Nb and thermophoresis parameter Nt is shown in Fig. 5, which exhibits that the temperature rises as the increase of Brownian motion parameter Nb and thermophoresis parameter Nt, and the thickness of the thermal boundary layer also becomes thicker, which means that the thermal resistance enlarges.

The variation of the temperature profiles for different values of the thickness parameter a and shape parameter b is shown in Fig. 6. It can be obtained from Fig. 6 (a) and (b) that the temperature rises as the thickness parameter a and thickness parameter b become larger, which demonstrate a loss of the thickness of the thermal boundary layer. It is worth mentioning that the steepness has a more significant effect on the temperature curve.

The dependence of the concentration profiles for different values on the shape parameter b and Brownian motion parameter Nb is shown in Fig. 7. The concentration and the thickness of concentration boundary layer are observed to increase as the magnitude of the shape parameter b increases in Fig. 7 (a). The effect of Brownian motion parameter Nb on the concentration profile is displayed in Fig. 7 (b). The result shows that the Brownian motion parameter Nb enhances the concentration of nanofluid, together with the thickness

of concentration boundary layer.

Fig. 8 shows the variation of the radial and tangential velocity profiles for different values of the Reynolds number. In Fig. 8 (a), the values of the peak of radial velocity increase with the increasing Reynolds number Re, and its location moves slightly towards the disk. As the Reynolds number increases, the radial velocity boundary layer thickness becomes thinner. It is noted that the tangential velocity distribution shows decreasing behavior corresponding to higher values of Reynolds number. Higher values of the Reynolds number result in the reduction of tangential velocity boundary layer thickness as presented in Fig. 8 (b). Fig. 9 indicates the effects of the Reynolds number for the axial velocity. There is an enhancement in axial velocity near the disk while there is a reduction in axial velocity far away from the disk. It is observed that the boundary layer thickness decreases correspondingly.

Effects of the Reynolds number on temperature and concentration are captured in Fig. 10. There is a reduction in temperature and thermal layer thickness within the frame of Reynolds number Re. For higher Reynolds number, a reduced concentration of the nanofluid is considered in Fig. 10 (b). Therefore, the thickness of the concentration boundary layer becomes thinner and the ability of mass transfer is enhanced.

In Fig. 11, the variation of the local skin-friction coefficient and the local Sherwood number for different values of the thickness parameter a and the shape parameter b. Fig. 11 (a) shows that there is an increase in the local skin-friction coefficient with the increasing values of the thickness parameter a and shape parameter b. Fig. 11 (b) displays an increasing trend in the profile of local Sherwood number is observed at all values of the thickness parameter a and shape parameter b. A high local Sherwood number indicates that the intensity of fluid convective mass transfer near the disk is enhanced. The change of skin friction coefficient is nonlinear with shape parameter, while the growth of local Sherwood number is the approximately linear correlation.

Fig. 12 illustrates the variation of local Nusselt number and the local Sherwood number for different values of the Brownian motion parameter Nb and thermophoresis parameter Nt. It is evident that the local Nusselt number is seen to be sufficiently reduced for Brownian motion parameter Nb and thermophoresis parameter Nt increase in Fig. 12 (a). However, the local Sherwood number rises as the values of Brownian motion parameter Nb and thermophoresis parameter Nt increase in Fig. 12 (b). It is worth mentioning that the local Sherwood number presents nonlinear growth with the Brownian motion.

Finally, Table 3 describes the effect of thickness parameter a and shape parameter b variations on the local Nusselt number. As the thickness parameter a increase, there is a rise in the local Nusselt number at the disk. But, an increase in the thickness number b leads to a decrease in local Nusselt number. Physically, a thinner disk with steeper surface results in small heat transfer rate.

4. Conclusions

Boundary layer flow of two-phase nanofluid over a rotating disk with exponential variable thickness in porous media has been studied. The generalized Von Karman transformation

is used to convert the partial differential equations into a system of nonlinear ordinary differential equations that can be solved numerically by bvp4c in Matlab. Comparison with previous solutions is also made to ensure the accuracy and efficiency of the applied numerical technique. Related physical parameters (thickness parameter a, shape parameter b, permeability parameter M, Brownian motion parameter Nb and thermophoresis parameter Nt) are analyzed graphically. Key points of the present study are listed below:

(I) With the increase of shape parameter b, the radial velocity first decreases and then increases, showing the opposite trend on the sides of the peak value.

(II) Temperature rises as both the thickness parameter a and shape parameter b become larger.

(III) Temperature and concentration profiles decline with an increase of Brownian motion parameter Nb. At the same time, their boundary layers also become thicker.

(IV) The thickness parameter a enhances the heat transfer rate of the disk while shape parameter b decreases the heat transfer rate.

Acknowledgments

The work of the authors is supported by the National Natural Science Foundations of China (nos. 11772046, 11771040).

5. References

[1] Chol, S.U. S. and Estman, J.A. (1995), "Enhancing thermal conductivity of fluids with nanoparticles", *ASME-Publications-Fed*.

[2] Eastman, J.A., Choi, S.U. S., Li, S., Yu, W. and Thompson, L. J. (2001), " Anomalously increased effective thermal conductivities of ethylene glycol-based nanofluids containing copper nanoparticles", *Applied physics letters*, Vol. 78 No. 6, pp. 718-720.

[3] Buongiorno, J. (2006), " Convective Transport in Nanofuids", *Journal of heat transfer*, Vol. 128 No. 3, pp. 240-250.

[4] Kuznetsov, A.V. and Nield, D. A. (2010), "Natural convective boundary-layer flow of a nanofuid past a vertical plate", *International Journal of Thermal Sciences*, Vol. 49 No. 2, pp. 243-247.

[5] Sheikholeslami, M., Gorji-Bandpy, M. and Soleimani, S. (2013), " Two phase simulation of nanofuid flow and heat transfer using heatline analysis", *International Communications in Heat & M*ass Transfer, Vol. 47 No. 5, pp. 73-81.

[6] Reddy, P.S. and Chamkha, A. (2017), "Heat and mass transfer analysis in natural convection flow of nanofluid over a vertical cone with chemical reaction", *International Journal of Numerical Methods for Heat & Fluid Flow*, Vol. 27 No.1, pp. 2-22.

[7] Nield, D.A. and Kuznetsov, A.V. (2011), "The Cheng-Minkowycz problem for the double-diffusive natural convective boundary layer flow in a porous medium saturated by a nanofluid", *International Journal of Heat and Mass Transfer*, Vol. 54 No.1-3, pp. 374-378.

[8] Chamkha, A., Abbasbandy, S. and Rashad, A.M. (2015), "Non-Darcy natural convection flow for non-Newtonian nanofluid over cone saturated in porous medium with uniform heat and volume fraction fluxes", *International Journal of Numerical Methods for Heat & Fluid Flow*, Vol. 25 No.2, pp. 422-43.

[9] Zhang, Y., Zhang, M. and Bai, Y. (2016), "Flow and heat transfer of an Oldroyd-B nanofluid thin film over an unsteady stretching sheet", *Journal of Molecular Liquids*, Vol. 220, pp. 665-670.

[10] Zhang, Y., Zhang, M. and Bai, Y. (2017), "Unsteady flow and heat transfer of power-law nanofluid thin film over a stretching sheet with variable magnetic field and power-law velocity slip effect", *Journal of the Taiwan Institute of Chemical Engineers*, Vol. 70, pp. 104-110.

[11] Wakif, A., Boulahia, Z., Ali, F., Eid, M.R. and Sehaqui, R. (2018), "Numerical Analysis of the Unsteady Natural Convection MHD Couette Nanofluid Flow in the Presence of Thermal Radiation Using Single and Two-Phase Nanofluid Models for Cu-Water Nanofluids", *International Journal of Applied and Computational Mathematics*, Vol. 4 No. 3, pp. 81.

[12] Khayargoli, P., Loya, V., Lefebvre, L.P. and Medraj,M. (2004, June), "The impact of microstructure on the permeability of metal foams", in: CSME forum, Vol. 2004, pp. 220-228.

[13] Yih, K.A. (1998), "The effect of uniform suction/blowing on heat transfer of magnetohydrodynamic Hiemenz flow through porous media", *Acta Mechanica*, Vol. 130 No. 3-4, pp. 147-158.

[14] Chamkha, A.J. and Al-Humoud, J.M. (2007), "Mixed convection heat and mass transfer of non-Newtonian fluids from a permeable surface embedded in a porous medium", *International Journal of Numerical Methods for Heat & Fluid Flow*, Vol. 17 No. 2, pp. 195-212.

[15] Hassanien, I.A. and Al-Arabi, T.H. (2009), "Non-Darcy unsteady mixed convection flow near the stagnation point on a heated vertical surface embedded in a porous medium with thermal radiation and variable viscosity", *Communications in Nonlinear Science and Numerical Simulation*, Vol. 14 No. 4, pp. 1366-1376.

[16] J. Chamkha, A., Mallikarjuna, B., Bhuvana Vijaya, R. and Prasada Rao, D.R. V. (2014), "Heat and mass transfer in a porous medium filled rectangular duct with Soret and Dufour effects under inclined magnetic field", *International Journal of Numerical Methods for Heat & Fluid Flow*, Vol. 24 No. 7, pp. 1405-1436.

[17] Barnoon, P. and Toghraie, D. (2018), "Numerical investigation of laminar flow and heat transfer of non-Newtonian nanofluid within a porous medium", *Powder Technology*, Vol. 325, pp.78-91.

[18] Karman, T.V. (1921), "Über laminare und turbulente Reibung", *ZAMM-Journal of Applied Mathematics and Mechanics/Zeitschrift für Angewandte Mathematik und Mechanik*, Vol. 1 No. 4, pp. 233-252.

[19] Millsaps, K. (1951), "Heat Transfer by Laminar Flow from a Rotating Plate", *Journal of the Aeronautical Sciences*, Vol. 18 No. 2, pp. 120-126.

[20] Ackroyd, J.A. D. (1978), "On the steady flow produced by a rotating disc with either surface suction or injection", *Journal of Engineering Mathematics*, Vol. 12 No. 3, pp. 207-220.

[21] Turkyilmazoglu, M. (2010), "Purely analytic solutions of magnetohydrodynamic swirling boundary layer flow over a porous rotating disk", *Computers & Fluids*, Vol. 39 No. 5, pp.

793-799.

[22] Devi, S.P. and Devi, R.U. (2012), "Effects of Thermal Radiation on Hydromagnetic Flow due to a Porous Rotating Disk with Hall Effect", *Journal of Applied Fluid Mechanics*, Vol. 5 No. 2, pp. 1-7.

[23] Rashidi, M.M., Abelman, S. and Mehr, N.F. (2013), "Entropy generation in steady MHD flow due to a rotating porous disk in a nanofluid", *International Journal of Heat and Mass Transfer*, Vol. 62, pp. 515-525.

[24] Khan, N.A., Khan, S., Shaikh, A. and Raja, M.A. Z. (2016), "MHD Stagnation Point Flow of Nanofluids Over an Off Centered Rotating Disk in a Porous Medium via Haar Wavelet", *Journal of Nanofluids*, Vol. 5 No. 3, pp. 444-458.

[25] Xun, S., Zhao, J., Zheng, L., Chen, X. and Zhang, X. (2016), "Flow and heat transfer of Ostwald-de Waele fluid over a variable thickness rotating disk with index decreasing", *International Journal of Heat and Mass Transfer*, Vol. 103 No. 103, pp. 1214-1224.

[26] Hayat, T., Rashid, M., Imtiaz, M. and Alsaedi, A. (2017), "Nanofluid flow due to rotating disk with variable thickness and homogeneous-heterogeneous reactions", *International Journal of Heat and Mass Transfer*, Vol. 113, pp. 96-105.

[27] Hayat, T., Javed, M., Imtiaz, M. and Alsaedi, A. (2017), "Double stratification in the MHD flow of a nanofluid due to a rotating disk with variable thickness", *European Physical Journal Plus*, Vol. 132 No. 3, pp. 146.

[28] Hayat, T., Rashid, M., Khan, M.I. and Alsaedi, A. (2018), "Melting heat transfer and induced magnetic field effects on flow of water based nanofluid over a rotating disk with variable thickness", *Results in Physics*.

[29] Hayat, T., Qayyum, S., Khan, M. I. and Alsaedi, A. (2018), "Entropy generation in magnetohydrodynamic radiative flow due to rotating disk in presence of viscous dissipation and Joule heating", *Physics of Fluids*, Vol. 30 No. 1, pp. 017101.

[30] Liu, C., Pan, M., Zheng, L., Ming, C. and Zhang, X. (2016), "Flow and Heat Transfer of Bingham Plastic Fluid over a Rotating Disk with Variable Thickness", *Zeitschrift Für Naturforschung A*, Vol. 71 No. 11, pp. 1003-1015.

[31] Mirzaei, D. and Dehghan, M. (2012), "New implementation of ML-BIE method for heat conduction analysis in functionally graded materials", *Engineering Analysis with Boundary Elements*, Vol. 36 No.4, pp. 511-519.

[32] Dehghan, M. and Abbaszadeh, M. (2016), "Proper orthogonal decomposition variational multiscale element free Galerkin (POD-VMEFG) meshless method for solving incompressible NavierCStokes equation", *Computer Methods in Applied Mechanics and Engineering*, Vol. 311, pp. 856-888.

[33] Dehghan, M. and Abbaszadeh, M. (2017), "The use of proper orthogonal decomposition (POD) meshless RBF-FD technique to simulate the shallow water equations", *Journal of Computational Physics*, Vol. 351, pp. 478-510.

[34] Kamranian, M., Dehghan, M. and Tatari, M. (2017), "An adaptive meshless local PetrovC-Galerkin method based on a posteriori error estimation for the boundary layer problems", *Applied Numerical Mathematics*, Vol. 111, pp. 181-196.

[35] Dehghan, M. and Abbaszadeh, M. (2018), "An upwind local radial basis functions-differential quadrature (RBF-DQ) method with proper orthogonal decomposition (POD) approach for solving compressible Euler equation", *Engineering Analysis with Boundary Elements*, Vol. 92,

pp. 244-256.

Figures

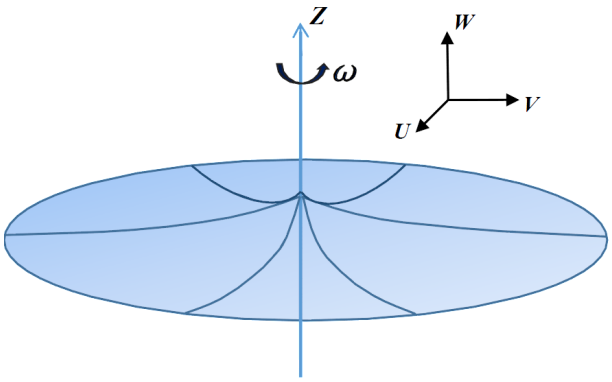

Fig. 1: Schematic diagram of the model.

Table 1: Comparison of $f'(0)$ for $b = 0$, $Re = 1$ with the previous works.

M	Turkyilmazoglu (2010) [21]	Rashidi et al. (2013) [23]	Present work
0	–	0.510186	0.509450
1	0.309258	0.309237	0.309253
4	0.165703	0.165701	0.165704

Table 2: The used CPU time(s) for the bvp4c and shooting method for momentum equations.

		$Re = 30$	$Re = 35$	$Re = 40$
CPU times (s)	bvp4c	0.089501	0.096779	0.108943
	shooting method	0.095570	0.107075	0.146863

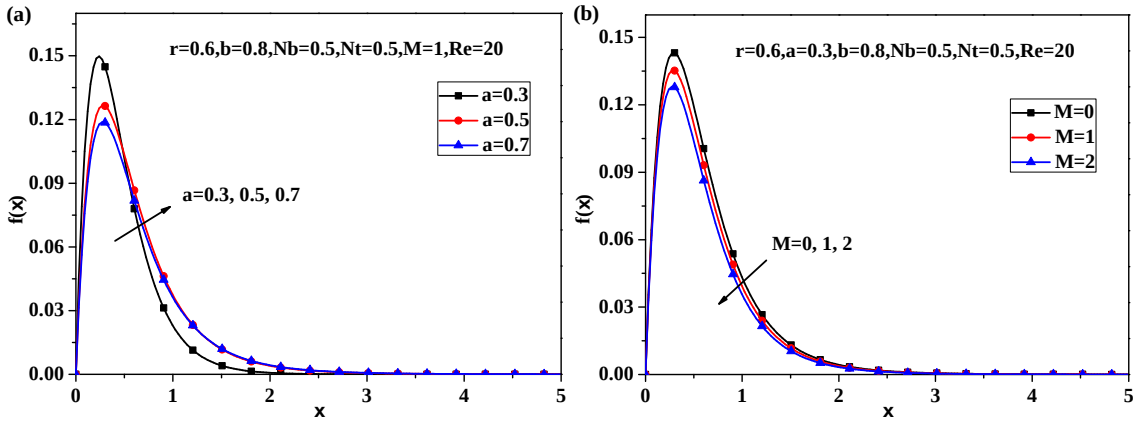

Fig. 2: Radial velocity profiles with the variation of thickness parameter and permeability parameter.

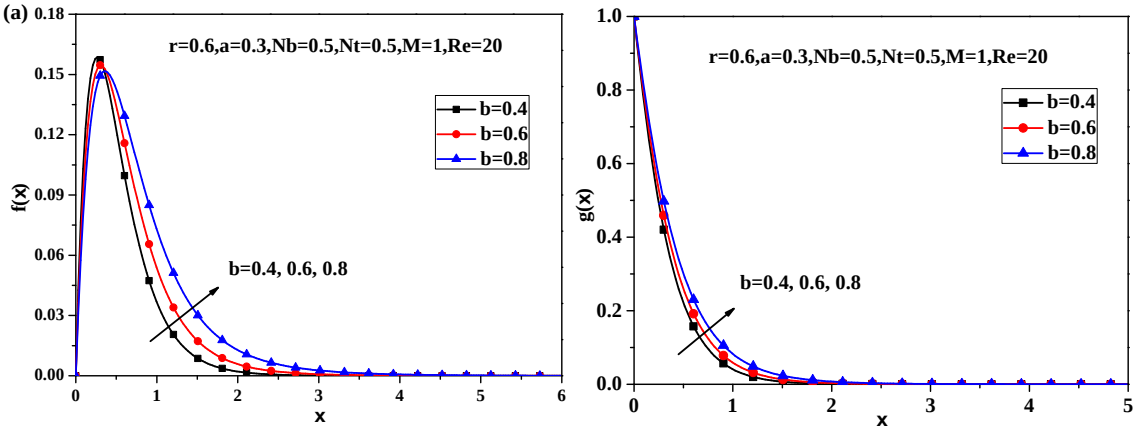

Fig. 3: Radial and tangential velocity profiles with the variation of shape parameter.

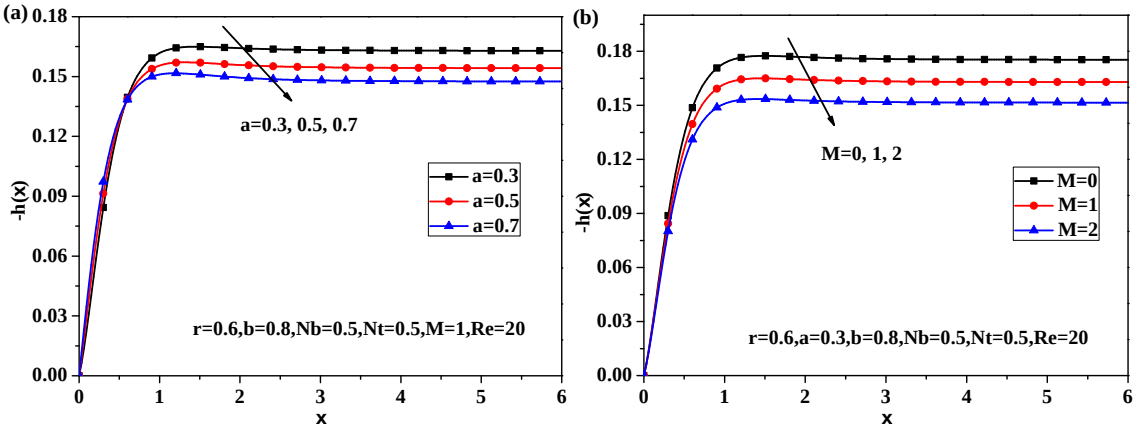

Fig. 4: Axial velocity profiles with the variation of thickness parameter and permeability parameter.

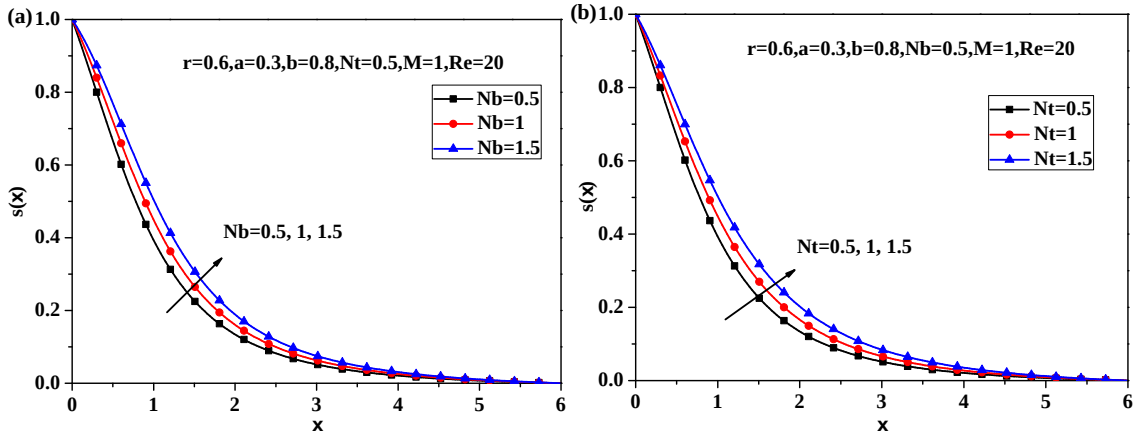

Fig. 5: Temperature profiles with the variation of Brownian motion parameter and thermophoresis parameter.

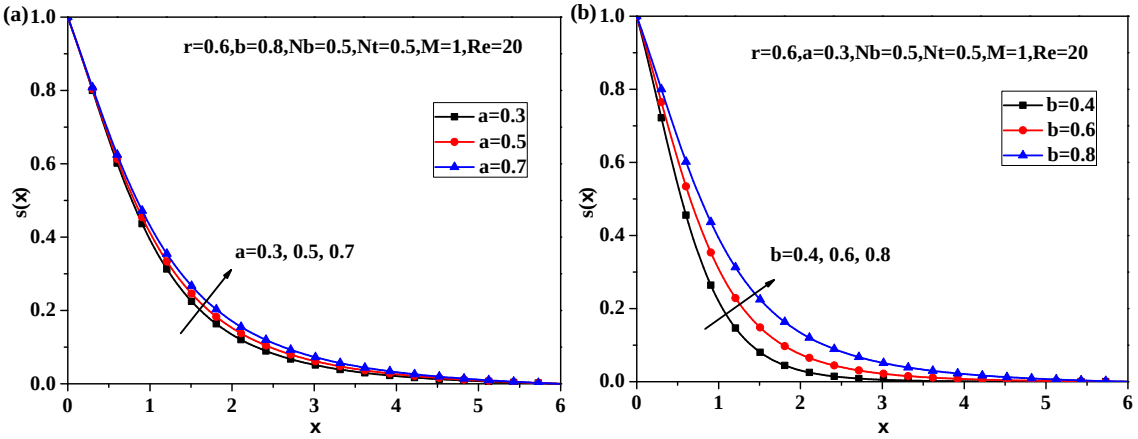

Fig. 6: Temperature profiles with the variation of thickness parameter and shape parameter.

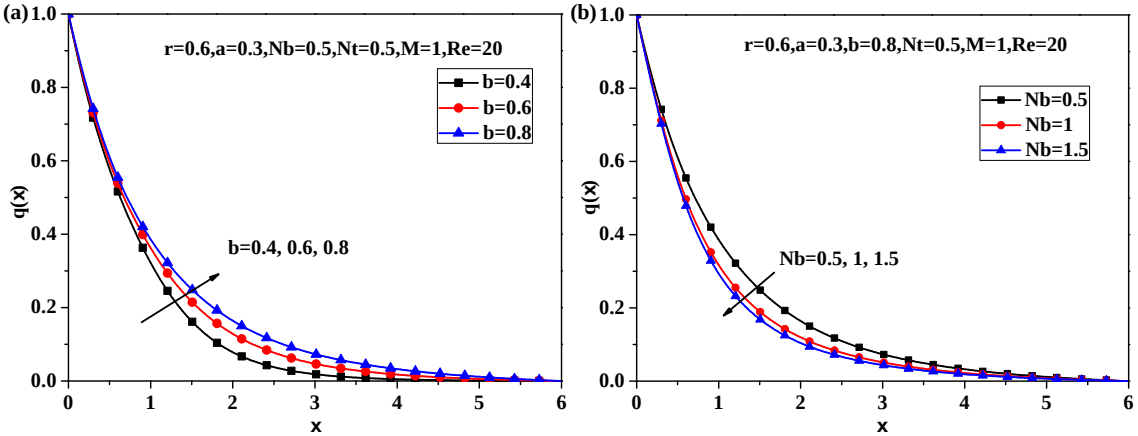

Fig. 7: Concentration profiles with the variation of shape parameter and Brownian motion parameter.

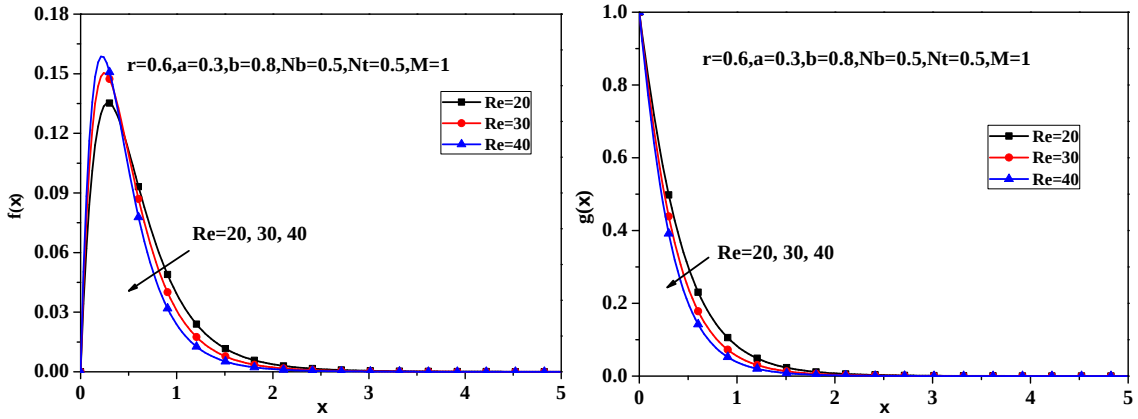

Fig. 8: Radial and tangential velocity profiles with the variation of Reynolds number.

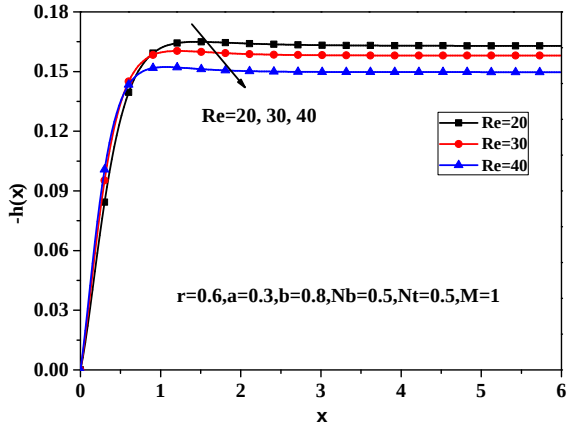

Fig. 9: Axial velocity profiles with the variation of Reynolds number.

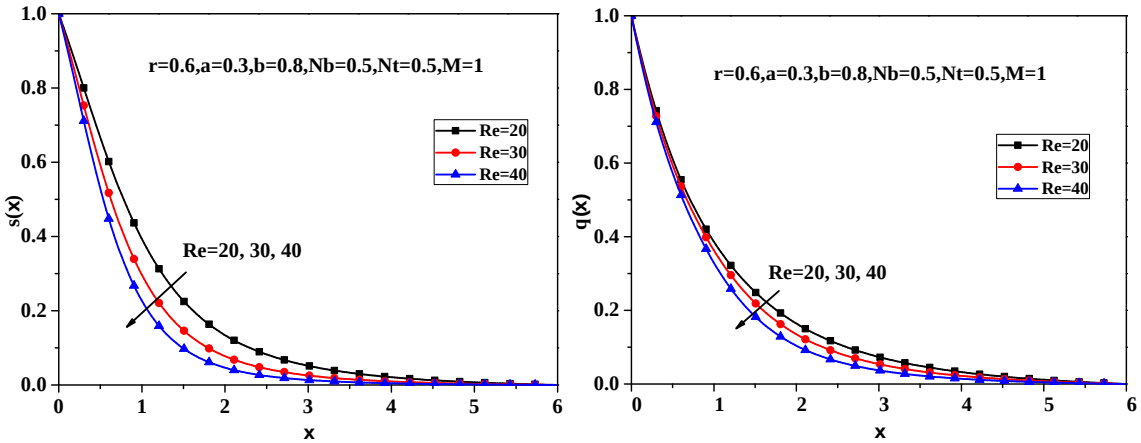

Fig. 10: Temperature and concentration profiles with the variation of Reynolds number.

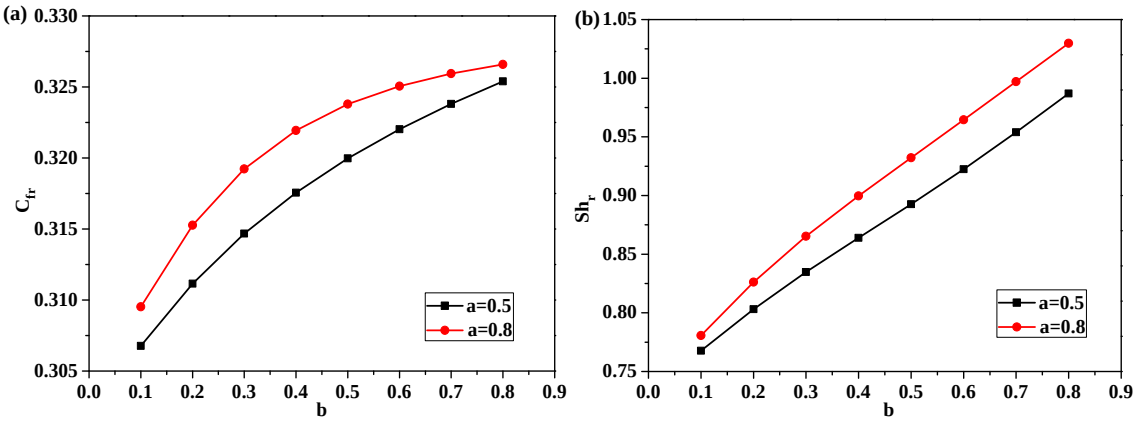

Fig. 11: Physical quantities at the disk with the variation of thickness parameter and shape parameter.

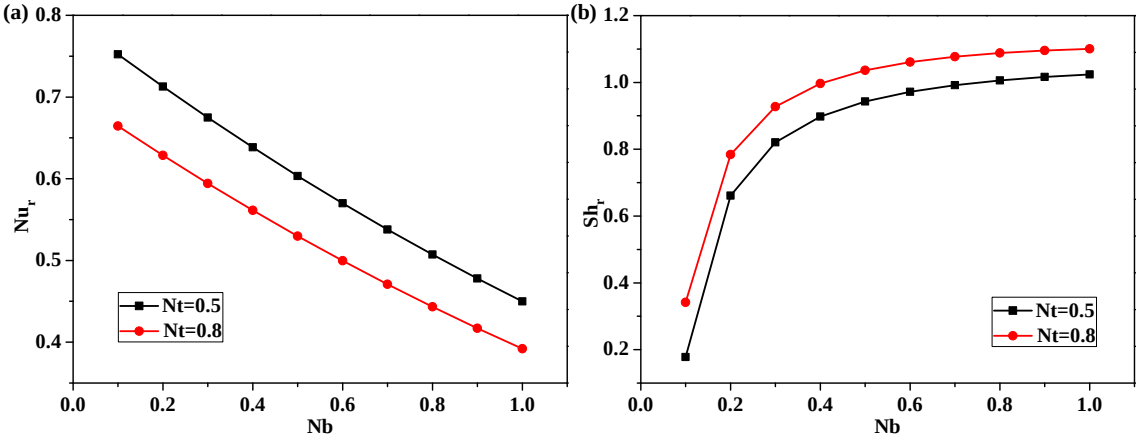

Fig. 12: Physical quantities at the disk with the variation of Brownian motion parameter and thermophoresis parameter.

Table 3: Local Nusselt number Nu_r for various values of a and b.

		b				
Nu_r		0.1	0.2	0.3	0.4	0.5
a	0.3	0.6713	0.66328	0.65428	0.64447	0.63405
	0.5	0.673	0.66543	0.65609	0.64551	0.63419
	0.7	0.67504	0.66689	0.65546	0.64215	0.62816